iScience

CellPress
OPEN ACCESS

Article

In situ and tunable structuring of semiconductor-in-glass transparent composite

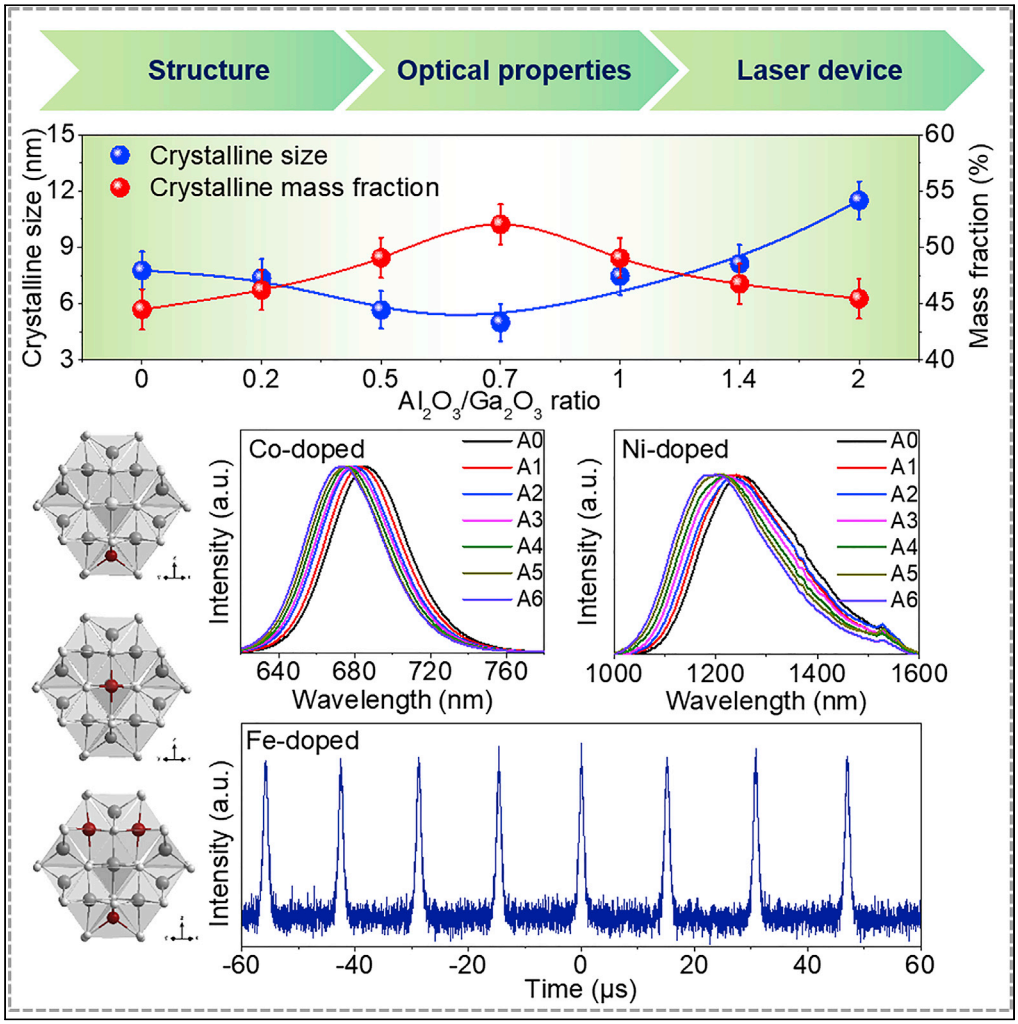

Liting Lin, Rulin Miao, Wenqiang Xie, ..., Jianrong Qiu, Haohai Yu, Shifeng Zhou

haohaiyu@sdu.edu.cn (H.Y.)
zhoushifeng@scut.edu.cn (S.Z.)

Highlights

In situ and tunable structuring of semiconductor-in-glass composites are presented

The composites can host various active dopants and show broadband optical response

A pulse laser at 2 μm based on Fe-doped composite is achieved for the first time

Lin et al., iScience 24, 101984
January 22, 2021
https://doi.org/10.1016/j.isci.2020.101984

iScience

CellPress
OPEN ACCESS

Article

In situ and tunable structuring of semiconductor-in-glass transparent composite

Liting Lin,[1,2,7] Rulin Miao,[3,7] Wenqiang Xie,[4,7] Jiejie Chen,[1,2,7] Yujun Zhao,[4,7] Zhenping Wu,[5,7] Jianrong Qiu,[6,7] Haohai Yu,[3,7,8,*] and Shifeng Zhou[1,2,7,8,*]

Summary

Semiconductor-in-glass composites are an exciting class of photonic materials for various fundamental applications. The significant challenge is the scalable elaboration of composite with the desirable combination of tunable structure, high semiconductor loading ratio, and excellent transparency. Here we report that the topological engineering strategy via hybridization of the glass network former enables to surmount the aforementioned challenge. It not only facilitates the *in situ* precipitation of $(Ga_{2-x}Al_x)O_3$ domains with continuously tunable composition but also allows to simultaneously refine the grain size and enhance the crystallinity. In addition, the composites exhibit excellent transparency and can host various active dopants. We demonstrate the attractive broadband optical response of the composite and achieve the pulse laser operation in mid-infrared waveband. The findings are expected to provide a fundamental principle of *in situ* modification in hybrid system for generation of high-performance semiconductor-in-glass composites.

Introduction

Transparent composites embedded with semiconductor nanostructures are of great interest in a wide range of fundamental applications, including smart electrochromic window, optical signal amplification, light-emitting diode, and quantum information processing (Brovelli et al., 2012; Sirleto et al., 2012; Llordes et al., 2013; Llordes et al., 2016; Henderson et al., 2011). Anecdotal evidences have confirmed that the performance of the resultant composite is cooperatively dominated by the bonding configuration of semiconductor domains and their existing form (e.g., density and distribution) inside the composite. Despite the great success in incorporation of various semiconductor categories into amorphous matrix, it still remains a long-standing challenge to prepare dense transparent composite with tunable microstructure. The most popular method of co-melting the semiconductor with the stable glass system followed by thermally induced precipitation usually restricts the available structure and density (Liu et al., 2018; Xia et al., 2019). This is mainly due to the low solubility of semiconductor in the employed host and difficulty in controlling the crystallization manner. The attempts to directly incorporate the predesigned semiconductors with diverse structures into glass matrix may potentially achieve high-density composite (Liu et al., 2017). Unfortunately, this approach can only be adapted to the solution environment, which usually causes undesired optical loss associated with hydroxyl or organic groups. New and effective strategy that overcomes these fundamental limitations could significantly advance the development of transparent composite.

Here, we propose topological engineering in glass matrix for simultaneous in situ structuring and enhancing loading ratio of semiconductor domains. The approach not only helps to achieve transparent composite embedded with continuously adjustable semiconductor alloy domains but also enables to reach a loading ratio of ~52.05%. As a result, the interesting optical response with finely tunable absorption and luminesce in the visible, infrared, and mid-infrared region can be realized. Furthermore, we also demonstrate the application of the collaborated composite for generating pulse laser in mid-infrared waveband for the first time.

Results and discussion

Design and preparation of semiconductor-in-glass transparent composites

Our strategy to explore novel transparent composite embedded with dense and structured semiconductor mainly involves the topological engineering of the glass matrix. It mainly includes two major design

[1]State Key Laboratory of Luminescent Materials and Devices, School of Materials Science and Engineering, South China University of Technology, Guangzhou 510640, China

[2]Guangdong Provincial Key Laboratory of Fiber Laser Materials and Applied Techniques, Guangdong Engineering Technology Research and Development Center of Special Optical Fiber Materials and Devices, Guangzhou 510640, China

[3]State Key Laboratory of Crystal Materials and Institute of Crystal Materials, Shandong University, Jinan 250100, China

[4]Department of Physics, South China University of Technology, Guangzhou 510640, China

[5]State Key Laboratory of Information Photonics and Optical Communications & School of Science, Beijing University of Posts and Telecommunications, Beijing 100876, China

[6]College of Optical Science and Engineering, Zhejiang University, Hangzhou 310027, China

[7]These authors contributed equally

[8]Lead Contact

*Correspondence: haohaiyu@sdu.edu.cn (H.Y.), zhoushifeng@scut.edu.cn (S.Z.)

https://doi.org/10.1016/j.isci.2020.101984

principles. First, being different from the generally employed method in which semiconductor was introduced as doping agent, we tried to incorporate the target semiconductor as the primary component of the network former in glass. This may enable to improve the solubility of the semiconductor precursor. Second, we devoted our efforts to hybridize the network former. It was expected that the topological design in glass matrix by interpenetrating the network chain may provide new opportunity for simultaneously tuning the precipitation habit of semiconductor domains and in situ modifying their microstructure.

Guided by the aforementioned principle, we demonstrated the success for *in situ* and tunable structuring of a prototype semiconductor Ga_2O_3, which has gained great attention due to their significant technological applications such as transparent electrode, solar blind UV detector, solar-cell energy conversion, and high-temperature gas sensors (Stepanov et al., 2016; Pearton et al., 2018; Chen et al., 2019; Xie et al., 2019). A systematic screening of the glass-forming ability of various glass systems (tellurite, phosphor, silicate, and germanate) containing Ga_2O_3 was examined. It was found that homogeneous glasses can be obtained based on SiO_2-Ga_2O_3 via fast melting-quenching processing, implying the excellent solubility of Ga_2O_3 in this system (Ceccato et al., 2001; Zhou et al., 2013). Furthermore, Al_2O_3 can also be well incorporated into SiO_2-Ga_2O_3, mainly benefited from the great chemical affinity between Al_2O_3 and SiO_2/Ga_2O_3. Based on these facts, material candidates derived from SiO_2-Ga_2O_3-Al_2O_3 with different Al_2O_3/Ga_2O_3 ratios of 0, 0.2, 0.5, 0.7, 1.0, 1.4, and 2.0 were fabricated. The structure analysis based on Raman scattering spectrum (Figure S1, Supplemental information) indicated that both Ga_2O_3 and Al_2O_3 act as the glass network former in these system.

The transparent composites can be fabricated via simple heat treatment at 850°C for 2 h, and they are denoted as A0, A1, A2, A3, A4, A5, and A6 for Al_2O_3/Ga_2O_3 ratios of 0, 0.2, 0.5, 0.7, 1.0, 1.4, and 2.0, respectively. The microstructures of the samples were systematically studied. Figure 1A shows the X-ray powder diffraction (XRD) data of the composites and the standard diffraction patterns of Ga_2O_3 (JCPDS 00-020-0426) and $Al_{2.667}O_4$ (JCPDS 01-080-1385). The data show that the precipitated crystalline phase in sample A0 can be indexed to the pure γ-Ga_2O_3. In addition, the diffraction peaks gradually shift to the higher 2θ with the increase of Al_2O_3/Ga_2O_3 ratio, as evidenced in the enlarged region of 60°–69° (Figure 1B). It can be attributed to the substitution of Ga^{3+} by Al^{3+} in the Ga_2O_3 crystal lattice, because of the relative smaller ionic radius of Al^{3+} (0.53 Å) compared with that of Ga^{3+} (0.62 Å). The results confirm that Ga_2O_3 and Al_2O_3 are mutually soluble over the wide Al_2O_3/Ga_2O_3 ratio range and the composition-tunable γ-$(Ga_{2-x}Al_x)O_3$ semiconductor alloy domains can be precipitated via *in situ* crystallization. The Raman scattering spectra for all composites in the range of 180–900 cm^{-1} are given in Figure 1C. The observed characteristic bands can be classified into three groups: high-frequency stretching and bending of $[GaO_4]$/$[AlO_4]$ tetrahedra (600–800 cm^{-1}), the vibrations of the bridged oxygen Ga-O-Ga/Al-O-Al linkages (500–600 cm^{-1}), and mid-frequency deformation of $[Ga_2O_6]$/$[Al_2O_6]$ octahedra (310–480 cm^{-1}) (Rao et al., 2005; Yue et al., 2018). Notably, Raman peaks at 600–800 cm^{-1} waveband also gradually shift toward higher frequency region as the Al_2O_3/Ga_2O_3 ratio increases, giving additional evidence about the formation of semiconductor alloy domains. Figures 1D–1G show the transmission electron microscopic (TEM) images as well as the histograms of the domain sizes of A0 and A6 samples. As presented in Figures 1D and 1F, the semiconductor domains with a mean diameter of approximately ~7.81 and 11.37 nm are homogeneously distributed in the glass matrix. The corresponding high-resolution TEM images exhibit clear lattice fringe, which is estimated to be ~0.250 and 0.244 nm in samples A0 and A6, respectively. They can be ascribed to the d(311) spacing of γ-$(Ga_{2-x}Al_x)O_3$ according to the XRD pattern. The average crystalline size and mass fraction for various samples were calculated and exhibited in Figure 1H. It is evident that the crystalline size of γ-$(Ga_{2-x}Al_x)O_3$ semiconductor alloy domains first decreases with the Al_2O_3/Ga_2O_3 ratio and then increases. The crystallite size is 7.77 nm for pure Ga_2O_3, and it decreases to 4.99 nm when the Al_2O_3/Ga_2O_3 ratio is 0.7. As the Al_2O_3/Ga_2O_3 ratio surpasses 0.7, the crystallite size increases gradually and reaches a maximum value of 11.50 nm. In contrast, the crystalline mass fraction exhibits the opposite change trend, and it increases from 44.48% to 52.05% when the Al_2O_3/Ga_2O_3 ratio changes from 0 to 0.7, and then decreases to 45.45% with increasing Al_2O_3/Ga_2O_3 ratio up to 2.0.

The observed phenomena can be explained based on two physical mechanisms. On one hand, the crystallization thermodynamics theory indicates that the grain growth is mainly affected by the interface energy, which is the energy difference between the energy level of the interface and that of the interior. It is an effective way to prevent the grain growth by the reduction of the interface energy (Maciel et al., 2003). It is supposed that the substitution of Al^{3+} for Ga^{3+} in the Ga_2O_3 lattice structure might create extra defects

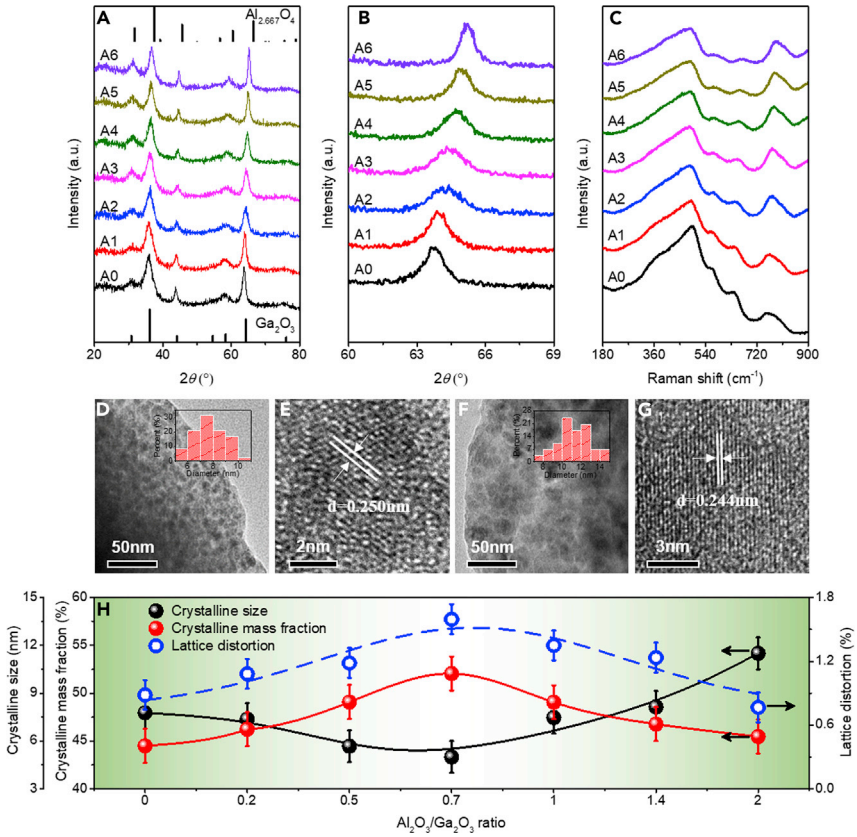

Figure 1. Structural analysis of transparent composites

(A) XRD patterns of the composites with various Al_2O_3/Ga_2O_3 ratios. The standard diffraction patterns of Ga_2O_3 and $Al_{2.667}O_4$ are sketched by referring to JCPDS cards (Nos. 00-020-0426 and 01-080-1385).

(B) Enlarged image of XRD from 60° to 69°.

(C) Raman spectra of the composites with various Al_2O_3/Ga_2O_3 ratios.

(D–G) TEM images and high-resolution TEM images of sample A0 (D and E) and A6 (F and G). The insets show the histograms of the size distribution of semiconductor alloy domain.

(H) Crystalline size (black sphere), crystalline mass fraction (red sphere), and lattice distortion (blue circle) versus Al_2O_3/Ga_2O_3 ratio.

and distortion, which may change the interface energy. According to the definition of the interface energy, the actual interface energy (γ_{actual}) of semiconductor alloy domains can be calculated based on the following relation (Huang and Yeh, 2010):

$$\gamma actual = \gamma - U \qquad \text{(Equation 1)}$$

where γ is the interface energy with distortion-free interiors and U is the lattice distortion strain energy, which increases with the lattice distortion $(\varepsilon^2)^{0.5}$. The lattice distortion can be calculated according to the Hall-Williamson method (Bukaemskiy et al., 2006). In this case, the lattice distortion is related to the inhomogeneous deformation of γ-$(Ga_{2-x}Al_x)O_3$ lattice. For details, the pure Ga_2O_3 and Al_2O_3 is expected to have the smallest lattice distortion; In $(Ga_{2-x}Al_x)O_3$ semiconductor alloy domains, the lattice distortion gets enhanced when the ratio of Al_2O_3/Ga_2O_3 in the γ-$(Ga_{2-x}Al_x)O_3$ semiconductor alloy domains is close to the value of 1 and then decreases upon further increase of Al_2O_3/Ga_2O_3 ratio. Therefore, the lattice distortion has a maximum, as shown in Figure 1H. As a consequence, the actual interface energy (γ_{actual}) of semiconductor alloy domains first decreases and then increases and reaches a minimum in sample A3 (i.e., Al_2O_3/Ga_2O_3 ratio = 0.7), which is in agreement with the change of the crystalline size. These results confirm that the lattice distortion reduces actual interface energy and helps to hinder the grain growth. At the same time, the lattice distortion may simultaneously act as potential heterogeneous nucleation sites and drive the nucleation process, thus improving the crystalline mass fraction (Figure 1H) (Rao et al., 2018). On the other hand, the addition of Al_2O_3 increases the configurational entropy of the semiconductor

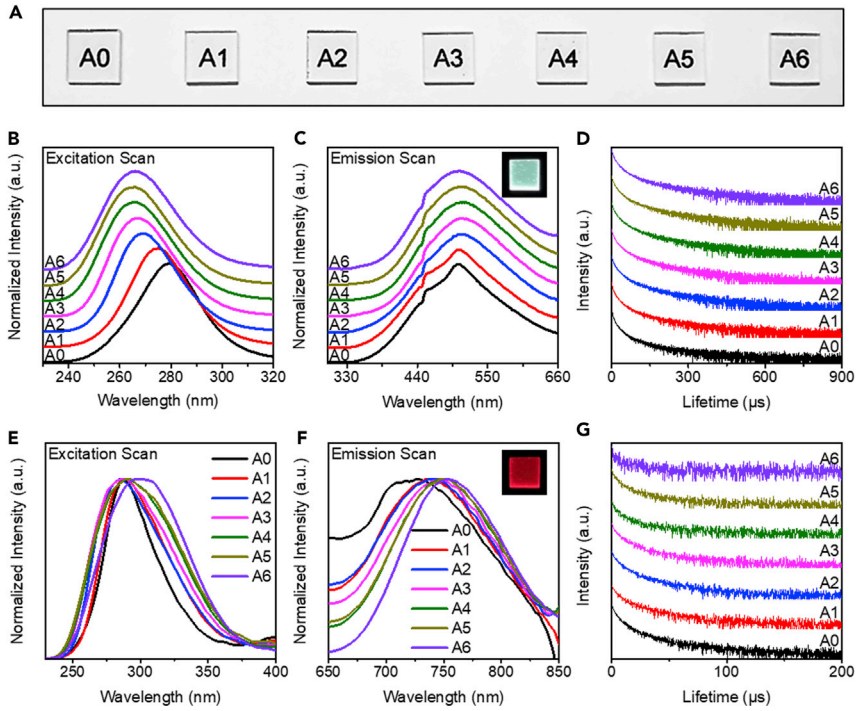

Figure 2. Optical properties of transparent composites

(A) Photographs of the transparent composites.

(B–D) The luminescence (B and C) and decay curves (D) of blue-green luminescence. Insets: the luminescence photograph with blue-green emission for sample A6.

(E–G) The luminescence (E and F) and decay curves (G) of red luminescence. Insets: the luminescence photograph with red emission for sample A6.

domains, and this "enhanced entropy effect" may hinder the growth of domains due to the sluggish atomic diffusion. This mechanism has been confirmed in high-entropy system (Yang et al., 2016). As a result, the highest density and smallest particle size of semiconductor alloy domains can be simultaneously achieved in transparent composites by hybridizing the network former in glass.

Optical properties of transparent composites

The obtained transparent composites are highly transparent (Figures 2A and S2, Supplemental information), implying their promising applications in photonics. According to defect chemistry, substitutional replacement of Ga^{3+} with Al^{3+} may tailor the band structures in the semiconductor domains, thus potentially imparting new optical properties to the composites. Photoluminescence excitation (PLE), photoluminescence (PL) spectroscopy, and luminescence decay measurements were employed to study the luminescence features of transparent composites, and the results are displayed in Figures 2B–2G. Under excitation with UV light, all composites show intense blue-green luminescence with the maximum at around 506 nm (Figures 2B and 2C). The excitation spectra of the blue-green luminescence exhibit a notable blue-shift with increasing Al_2O_3/Ga_2O_3 ratio, because of the enlarged optical band gap of Al-doped Ga_2O_3 compared with that of pure Ga_2O_3 (Ma et al., 2017). Interestingly, only a slight shift can be observed in the luminescence spectra, which could be ascribed to the donor-acceptor pairs (DAP) recombination nature of the radiation transition. The DAP is composed of an electron trapped on a donor due to oxygen vacancies (V_O) and a hole trapped on an acceptor due to gallium ion vacancy (V_{Ga}) or a pair of charged vacancies (V_O-V_{Ga}) in Ga_2O_3 (Binet and Gourier, 1998). The photon energy of the luminescence is governed by the DAP separation distance. According to Wang et al. (2010), DAP separation distance is affected by many factors, including the defect inside the Ga_2O_3 semiconductor and the crystalline size. In our case, with the change of Al_2O_3/Ga_2O_3 ratio, the size and density of semiconductor domain also change. So it might be supposed that many factors collaboratively contribute to affect the DAP separation distance, and as a consequence, the emission band of the composites only shows slight shift. With

increasing Al_2O_3/Ga_2O_3 ratio, the emission intensity of blue-green luminescence first decreases and then increases (Figure S3A, Supplemental information). The decay curves of the blue-green luminescence are shown in Figure 2D. The decay lifetime can be calculated based on the decay dynamics, and it is significant to note that the emission lifetime extends from 37.23 μs (A0) to 50.02 μs (A6) with increased Al_2O_3/Ga_2O_3 ratio.

In addition, a strong red luminescence can also be observed in the composites. The PLE and PL spectra of the red luminescence are shown in Figures 2E and 2F, respectively. It is seen that both the excitation and emission spectra shift to long wavelength with the increase of Al_2O_3/Ga_2O_3 ratio and the full width at half maximum of excitation spectra increases. Notably, it is the first time to observe that Al alloying may help to tune the red luminescence of Ga_2O_3 semiconductor domains. However, the red luminescence mechanism of composites is still unclear. Zhang et al. indicated that the red emission can be ascribed to the electron-hole recombination via the vicinity donors and acceptors (Zhang et al., 2006). It is also reported that red emission bands in β-Ga_2O_3 nanostructures can be correlated with the subband formed by amorphous Ga_2O_3 (Zhou et al., 2007), whereas Chang et al. suggested that the presence of red emission is due to nitrogen doping (Chang et al., 2011). Based on our investigations, the Al-doped Ga_2O_3 may generate a deep acceptor level in the band gap, and the observed red luminescence of semiconductor domains is likely due to the recombination transition involving a nearby DAP of V_O and deep acceptor level. The increase of Al^{3+} doping level will lead to form a dopant subband in the band gap and decrease the DAP separation distance, resulting in a shift of the red emission to the lower energies as shown in Figure 2F (Song et al., 2004). The emission intensity of red luminescence gradually increases with increasing Al_2O_3/Ga_2O_3 ratio (Figure S3B, Supplemental information). The decay dynamics of the red luminescence was also characterized, and the results are shown in Figure 2G. Both decay curves can be fitted by exponential functions, and the estimated lifetimes are ~30 μs for samples A0~A5 and 17.74 μs for sample A6.

Optical properties of transition-metal ion-doped transparent composites

Doping of semiconductor alloy constitutes an efficient approach for tuning the electrical, optical, magnetic, and catalytic properties. In the next step, we further tried to introduce various active dopants to demonstrate the possibility of optical property control via *in situ* structuring in semiconductor-in-glass transparent composite. As the proof-of-concept experiment, the transition-metal ion species (Co, Ni, and Fe) were selected as the prototype dopants and introduced into the homogeneous glass. The doped transparent composites were fabricated via heat treatment at the appropriate temperatures as indicated above (Figure S4, Supplemental information). Spectral analysis indicates a notable contrast in the absorption features of as-made glass and composite, confirming the success in incorporation of dopants into semiconductor alloy domains (Figure S5, Supplemental information). Figure 3 shows the proposed doping model and the absorption and luminescence spectra of the corresponding transparent composites doped with Co, Ni, and Fe. Impressively, the spectral features of the transparent composite can be finely tuned via rational control of the Al_2O_3/Ga_2O_3 ratio. The detailed mechanism is discussed based on the electronic transitions of Co, Ni, and Fe.

In Co-doped transparent composites, the absorption bands at about 550, 590, and 640 nm in the visible region and 1,000–2,000 nm in the infrared region can be assigned to the fingerprint electronic transitions of $^4A_2(^4F) \rightarrow {}^2A_1(^2G)$, $^4A_2(^4F) \rightarrow {}^4T_1(^4P)$, $^4A_2(^4F) \rightarrow {}^2E(^2G)$, and $^4A_2(^4F) \rightarrow {}^4T_1(^4F)$ of $[CoO_4]^{6-}$, respectively (Figure 3B) (Lin et al., 2019). When excited with 532 nm, Co-doped samples show intense red luminescence at around 680 nm, which can be indexed to the $^4T_1(^4P) \rightarrow {}^4A_2(^4F)$ radiative transition of $[CoO_4]^{6-}$ (Figure 3C) (Volk et al., 2007). These results strongly suggest that Co^{2+} selectively incorporates into semiconductor alloy domains through substitution of tetrahedral Ga^{3+} (Figure 3A). Significantly, the characteristic absorption bands and emission bands of Co^{2+} exhibit gradual blue-shift with the increase of Al_2O_3/Ga_2O_3 ratio. From the electronic absorption spectra, the ligand field parameters of Co^{2+} ions in semiconductor domains were calculated using the Tanabe-Sugano matrix, and the results are presented in Table S1 (Supplemental information). It can be clearly observed that the crystal field strength (Dq) of Co^{2+} increases with the rise of Al_2O_3/Ga_2O_3 ratio. As a consequence, the energy gap between the excitation state and the ground state becomes larger, which causes the blue-shifts in the electronic transitions of Co^{2+} ions.

Similar phenomenon has also been observed in Ni-doped samples. As shown in Figure 3E, the absorption spectra exhibit an intense peak at around 370 nm and a broadband band between 570 and 700 nm, which can be assigned to the $^3A_2(F) \rightarrow {}^3T_1(P)$ and $^3A_2(F) \rightarrow {}^3T_1(F)$ electronic transitions of $[NiO_6]^{10-}$ (Moncorge

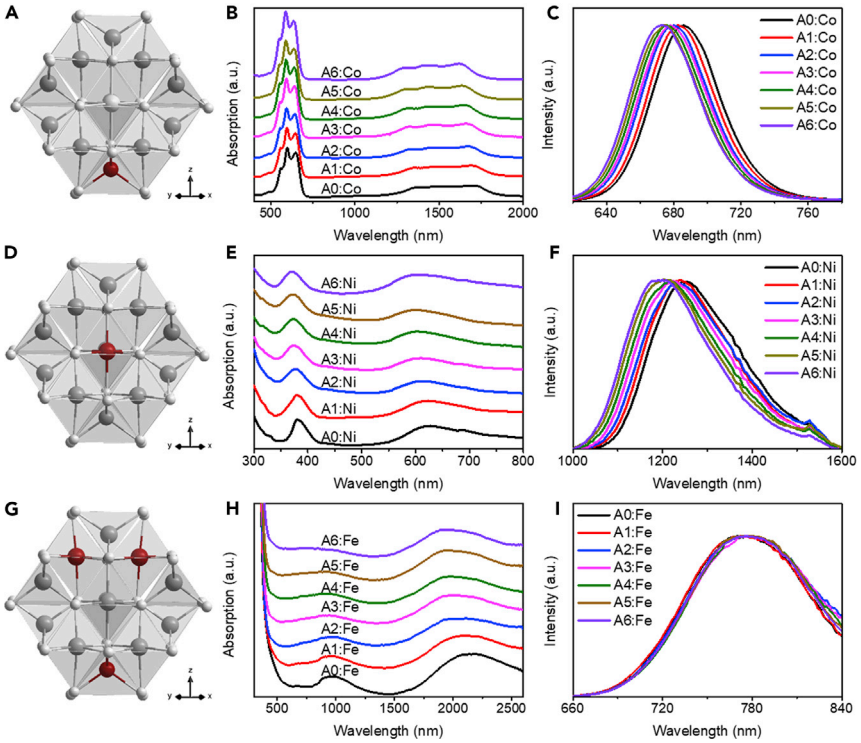

Figure 3. Structure model and optical properties of transition-metal ions (Co, Ni, and Fe)-doped transparent composites

(A–C) (A) Structure model, (B) absorption spectra, and (C) luminescence spectra of Co-doped samples.

(D–F) (D) Structure model, (E) absorption spectra, and (F) luminescence spectra of Ni-doped samples.

(G–I) (G) Structure model, (H) absorption spectra, and (I) luminescence spectra of Fe-doped samples. In the structure models, O, Ga/Al, and transition-metal atoms are colored in white, gray, and red, respectively.

and Benyattou, 1988; Zhou et al., 2013). Obviously, the peak position continuously shifts to the blue band region with the increase of Al_2O_3/Ga_2O_3 ratio. Under excitation of 808 nm, Ni-doped samples show intense near-infrared luminescence in 1,000–1,600 nm waveband region (Figure 3F), which can be attributed to the electronic transition of $^3T_2(F) \rightarrow {}^3A_2(F)$ (Zhou et al., 2013). Similar to the absorption features, the emission peaks also present obvious blue-shift from 1,256 to 1,196 nm. These results indicate that Ni^{2+} ions occupy octahedral position in semiconductor alloy domains (Figure 3D).

In addition, the optical properties of Fe-doped transparent composites have also been investigated. As shown in Figure 3H, the absorption bands at 700–1,250 nm and 1,500–2,600 nm waveband region correspond exactly to the $^5T_2 \rightarrow {}^5E$ transition of $[FeO_6]^{10-}$ and $^5E \rightarrow {}^5T_2$ transition of $[FeO_4]^{6-}$, respectively (Bingham et al., 2002). Under the excitation of 360 nm, Fe-doped samples exhibit intense red emission, which originates from the $^4T_1(^4G) \rightarrow {}^6A_1(^6S)$ transition of octahedral $[FeO_6]^{9-}$ (Figure 3I) (Pathak et al., 2014). These results indicate that there are two types of dopant centers, Fe^{2+} and Fe^{3+}, in the composite. Furthermore, it can be known that Fe^{2+} ion can simultaneously substitute for Ga^{3+} in the tetrahedral and octahedral sites, whereas Fe^{3+} ion may only incorporate into octahedral sites in the semiconductor domain (Figure 3G). Importantly, as the Al_2O_3/Ga_2O_3 ratio increases, the absorption bands of Fe^{2+} gradually shift to the shorter wavelengths. In contrast, the emission bands of Fe^{3+} only experience slight change, which may be associated with the fact that the electron configuration of Fe^{3+} is less sensitive to the local chemical environment.

Doping mechanism of transition-metal ions in transparent composites

To further clarify the doping mechanism of transition-metal ions in the semiconductor-in-glass transparent composite, we employed the density functional theory (DFT) for calculations of the local structure of Co^{2+} in γ-Ga_2O_3 and γ-$(Ga_{2-x}Al_x)O_3$ as our primary model system. As shown in Figure 4, DFT calculations show that the substitutional doping of Co^{2+} in pure γ-Ga_2O_3 and alloyed γ-$(Ga_{2-x}Al_x)O_3$ leads to the formation of different

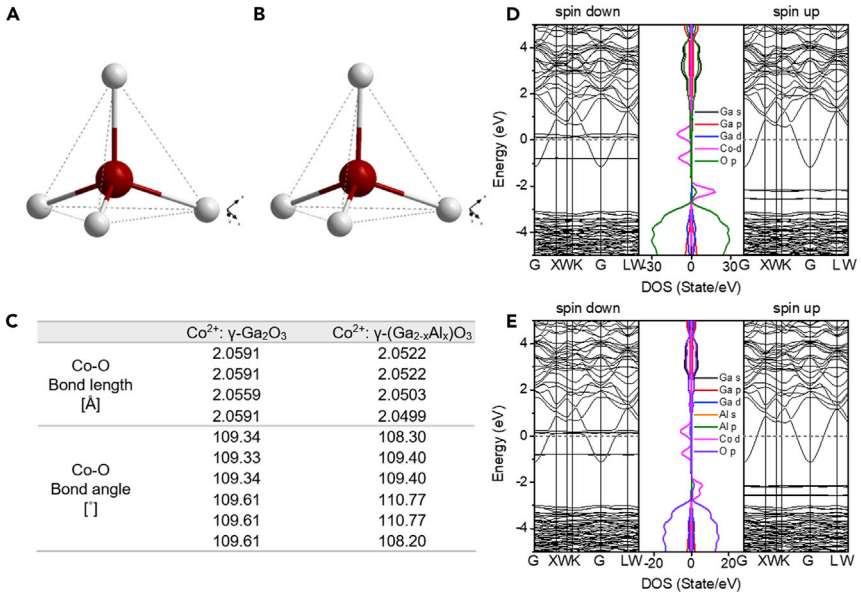

	Co^{2+}: γ-Ga_2O_3	Co^{2+}: γ-$(Ga_{2-x}Al_x)O_3$
Co-O Bond length [Å]	2.0591	2.0522
	2.0591	2.0522
	2.0559	2.0503
	2.0591	2.0499
Co-O Bond angle [°]	109.34	108.30
	109.33	109.40
	109.34	109.40
	109.61	110.77
	109.61	110.77
	109.61	108.20

Figure 4. Theoretical investigation on the doping mechanism

(A and B) Atomic configurations of [CoO_4] tetrahedron in pure γ-Ga_2O_3 (A) and alloyed γ-$(Ga_{2-x}Al_x)O_3$ (B). O atoms are colored in white, and Co atoms are colored in red.

(C) Calculated bond length and bond angle of [CoO_4] tetrahedron in pure γ-Ga_2O_3 and alloyed γ-$(Ga_{2-x}Al_x)O_3$.

(D and E) Computed electronic band dispersion and PDOS of Co^{2+}: γ-Ga_2O_3 (D) and Co^{2+}: γ-$(Ga_{2-x}Al_x)O_3$ (E).

[CoO_4] structural unit. Specifically, for Co^{2+} in pure γ-Ga_2O_3, the average bond length of Co-O is 2.058 Å and the average bond angle is 109.47° (Figures 4A and 4C). In contrast, for Co^{2+} in alloyed γ-$(Ga_{2-x}Al_x)O_3$, the average bond length of Co-O decreases slightly to 2.051 Å, and parts of bond angle change around ±1° after incorporation of Al^{3+} (Figures 4B and 4C). Based on the aforementioned calculations, the electronic structure and the partial densities of states (PDOS) of Co^{2+} in γ-Ga_2O_3 and γ-$(Ga_{2-x}Al_x)O_3$ can be obtained, and the results are shown in Figures 4D and 4E. Notably, Co^{2+} dopant additionally introduces electronic levels into the band gap of both γ-Ga_2O_3 and γ-$(Ga_{2-x}Al_x)O_3$. The PDOS clearly shows that these impurity levels originate from Co 3*d* orbitals. Moreover, the corresponding 3*d* orbitals split into t_2 and *e* orbitals, mainly associated with the strong interaction between Co ions and the matrix lattice. The calculated energy gap between t_2 and e orbitals is estimated to be 0.394 and 0.424 eV for Co^{2+} in γ-Ga_2O_3 and γ-$(Ga_{2-x}Al_x)O_3$, respectively. The results confirm that the crystal-field splitting energy (10 Dq) in γ-$(Ga_{2-x}Al_x)O_3$ is higher than that in γ-Ga_2O_3, which is well consistent with the experimental results estimated from absorption spectra.

Passive Q-switch performance of Fe-doped transparent composite

The intriguing optical response of the constructed transparent composites prompts us to further explore its application in photonics. As depicted in Figure 3, Fe-doped transparent composites exhibit a strong absorption band at 1,500–2,600 nm. This suggests their great potential as passive mid-infrared Q-switch for construction of mid-infrared pulse laser, which has been widely applied in molecule detection, environmental monitoring, and optical communication. To verify the proposal, the pulse lasing performance of the sample was evaluated by using the Tm-doped $YAlO_3$ (Tm: YAP) crystal as the laser gain medium. Figure 5A displays the schematic diagram of the experimental setup, and the detailed illustration can be found in the experimental section. Figures 5B and 5C show the output power and laser spectrum, respectively. As shown in the picture, the absorbed pump power threshold of the Q-switching is 0.49 W, and the average output power can be improved with the increasing absorbed pump power. The resultant slope efficiency is estimated to be ~30.85%. The maximum average output power of 0.24 W with the corresponding laser spectra peaking at 1,992 nm can be obtained at an absorbed pump power of 1.19 W. Figures 5D and 5E display the variations of repetition rate, pulse width, pulse energy, and peak power with the absorbed pump power. Obviously, with the enhancement of pump power, the repetition frequency, pulse energy, and peak power gradually increase, whereas the pulse width of laser first expands and then contracts. The typical pulse sequence with a repetition frequency of 66.82 kHz and shortest pulse width of 670 ns can be obtained under the absorbed pump power of 1.19 W, as presented in Figures 5F

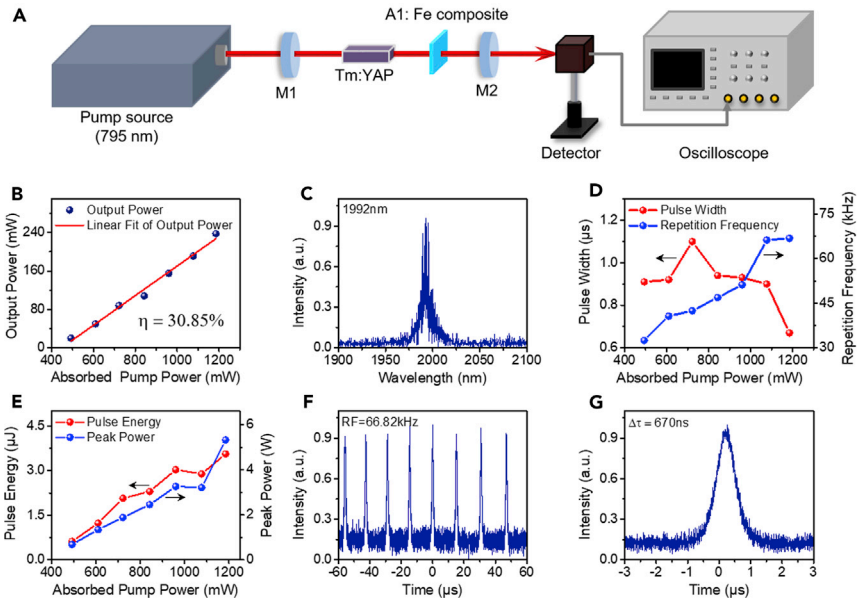

Figure 5. Pulse laser operation in the mid-infrared waveband

(A) Experimental schematic diagram.

(B) Average output power versus absorbed pump power.

(C) The spectrum of the output laser.

(D) Pulse width and repetition rate of the pulse laser versus absorbed pump power.

(E) Pulse energy and pulse peak power of the pulse laser versus absorbed pump power.

(F) Pulse train recorded by the oscilloscope.

(G) Single pulse with the pulse width of 670 ns.

and 5G. With the corresponding average output power of 0.24 W, repetition rate of 66.82 kHz, and pulse width of 670 ns, the maximum pulse energy and peak power can be calculated to be 3.56 μJ and 5.32 W, respectively. Therefore, Fe-doped transparent composite would be a promising passive Q-switch for 2 μm pulse laser generation and applications. Notably, to the best of our knowledge, this is the first report that transparent Fe-doped semiconductor-in-glass composite can be used as the saturable absorber to produce Q-switched laser in a Tm:YAP laser cavity. In addition, taking into account the tunable optical response feature of the sample, the pulse laser operation in a broad waveband in the mid-infrared region can be potentially realized.

Conclusion

We have demonstrated a novel strategy for *in situ* and tunable structuring of semiconductor-in-glass transparent composite, by topological engineering of the glassy phase. The topological control for hybridization of the glass network former enables to *in situ* and precisely tune the composition, size, and loading ratio of the embedded semiconductor domains. The elaborated transparent composites exhibit intriguing broadband optical response, and the application for generation of pulse laser operation in mid-infrared waveband has been demonstrated for the first time. It should be noted that the strategy should be universal to a wide category of semiconductor-in-glass transparent composite. Furthermore, our understanding of the *in situ* structure modification mechanism is greatly improved, offering new possibility to explore the extraordinary physical characteristics of semiconductor-in-glass composites and their new applications.

Limitations of the study

The effects of the Al_2O_3/Ga_2O_3 ratio on the passive Q-switch performance of Fe-doped transparent composites deserve to be further studied.

Resource availability

Lead contact

Further information and requests for resources and reagents should be directed to and will be fulfilled by the Lead Contact, Shifeng Zhou (zhoushifeng@scut.edu.cn).

Materials availability

Materials generated in this study are available from the Lead Contact with a completed Materials Transfer Agreement.

Data and code availability

The published article includes all datasets generated or analyzed during this study.

Methods

All methods can be found in the accompanying Transparent Methods supplemental file.

Supplemental information

Supplemental Information can be found online at https://doi.org/10.1016/j.isci.2020.101984.

Acknowledgments

The authors gratefully acknowledge financial support from the National Key R&D Program of China (2020YFB1805901), China; the National Natural Science Foundation of China (51972113, 51872095), China; Local Innovative and Research Teams Project of Guangdong Pearl River Talents Program (2017BT01X137), China; Key Program of Guangzhou Scientific Research Special Project (201904020013), China; Key R&D Program of Guangzhou (202007020003), China; Fundamental Research Funds for the Central University, China.

Author contributions

S.Z. proposed the idea and designed the experiments. L.L. prepared the samples. L.L., R.M., and J.C. were responsible for materials characterizations. W.X. and Y.Z. made the theoretical simulations. Y.Z., Z.W., J.Q., H.Y., and S.Z. evaluated the data. L.L., R.M., and S.Z. wrote the manuscript. All authors were involved in the discussion of the experiment results and in agreement with the content of manuscript.

Declaration of interests

The authors declare no competing interests.

Received: October 13, 2020
Revised: November 27, 2020
Accepted: December 17, 2020
Published: January 22, 2021

References

Binet, L., and Gourier, D. (1998). Origin of the blue luminescence of β-Ga_2O_3. J. Phys. Chem. Sol. *59*, 1241–1249.

Bingham, P.A., Parker, J.M., Searle, T., Williams, J.M., and Smith, I. (2002). Novel structural behaviour of iron in alkali–alkaline-earth–silica glasses. C. R. Chim. *5*, 787–796.

Brovelli, S., Chiodini, N., Lorenzi, R., Lauria, A., Romagnoli, M., and Paleari, A. (2012). Fully inorganic oxide-in-oxide ultraviolet nanocrystal light emitting devices. Nat. Commun. *3*, 690.

Bukaemskiy, A.A., Barrier, D., and Modolo, G. (2006). Physical properties of 8 mol% Ceria doped yttria stabilised zirconia powder and ceramic and their behaviour during annealing and sintering. J. Eur. Ceram. Soc. *26*, 1507–1515.

Ceccato, R., Dal Maschio, R., Gialanella, S., Mariotto, G., Montagna, M., Rossi, F., Ferrari, M., Lipinska-Kalita, K.E., and Ohki, Y. (2001). Nucleation of Ga_2O_3 nanocrystals in the K_2O-Ga_2O_3-SiO_2 glass system. J. Appl. Phys. *90*, 2522–2527.

Chang, L., Lu, T., Chen, Y., Yeh, J., and Shih, H.C. (2011). Effect of the doped nitrogen on the optical properties of β-Ga_2O_3 nanowires. Mater. Lett. *65*, 2281–2283.

Chen, X., Ren, F., Gu, S., and Ye, J. (2019). Review of gallium-oxide-based solar-blind ultraviolet photodetectors. Photon. Res *7*, 381–415.

Henderson, M.R., Gibson, B.C., Ebendorff-Heidepriem, H., Kuan, K., Afshar, V.S., Orwa, J.O., Aharonovich, I., Tomljenovic-Hanic, S., Greentree, A.D., Prawer, S., et al. (2011). Diamond in tellurite glass: a new medium for quantum information. Adv. Mater. *23*, 2806–2810.

Huang, P., and Yeh, J. (2010). Inhibition of grain coarsening up to 1000°C in (AlCrNbSiTiV)N superhard coatings. Scr. Mater. *62*, 105–108.

Lin, L., Wang, Y., Lan, B., Chen, J., Lv, S., Zhao, Y., Yu, H., Hao, J., Zhang, Q., Yang, Z., et al. (2019). Coordination geometry engineering in a doped disordered matrix for tunable optical response. J. Phys. Chem. C *123*, 29343–29352.

Liu, C., Li, Z., Hajagos, T.J., Kishpaugh, D., Chen, D.Y., and Pei, Q. (2017). Transparent ultra-high-loading quantum dot/polymer nanocomposite monolith for gamma scintillation. ACS Nano *11*, 6422–6430.

Liu, X., Zhou, J., Zhou, S., Yue, Y., and Qiu, J. (2018). Transparent glass-ceramics functionalized by dispersed crystals. Prog. Mater. Sci. *97*, 38–96.

Llordes, A., Garcia, G., Gazquez, J., and Milliron, D.J. (2013). Tunable near-infrared and visible-light transmittance in nanocrystal-in-glass composites. Nature *500*, 323–326.

Llordes, A., Wang, Y., Fernandez-Martinez, A., Xiao, P., Lee, T., Poulain, A., Zandi, O., Saez Cabezas, C.A., Henkelman, G., and Milliron, D.J. (2016). Linear topology in amorphous metal oxide electrochromic networks obtained via low-temperature solution processing. Nat. Mater. *15*, 1267–1273.

Ma, X., Zhang, Y., Dong, L., and Jia, R. (2017). First-principles calculations of electronic and

optical properties of aluminum-doped β-Ga_2O_3 with intrinsic defects. Results Phys. *7*, 1582–1589.

Maciel, A.P., Lisboa-Filho, P.N., Leite, E.R., Paiva-Santos, C.O., Schreiner, W.H., Maniette, Y., and Longo, E. (2003). Microstructural and morphological analysis of pure and Ce-doped tin dioxide nanoparticles. J. Eur. Ceram. Soc. *23*, 707–713.

Moncorge, R., and Benyattou, T. (1988). Excited-state absorption of Ni^{2+} in MgF_2 and MgO. Phys. Rev. B Condens. Matter *37*, 9186–9196.

Pathak, N., Gupta, S.K., Sanyal, K., Kumar, M., Kadam, R.M., and Natarajan, V. (2014). Photoluminescence and EPR studies on Fe^{3+} doped $ZnAl_2O_4$: an evidence for local site swapping of Fe^{3+} and formation of inverse and normal phase. Dalton Trans. *43*, 9313–9323.

Pearton, S.J., Yang, J., Cary, P.H., Ren, F., Kim, J., Tadjer, M.J., and Mastro, M.A. (2018). A review of Ga_2O_3 materials, processing, and devices. Appl. Phys. Rev. *5*, 011301.

Rao, R.F., Rao, A.M., Xu, B., Dong, J., Sharma, S., and Sunkara, M.K. (2005). Blueshifted Raman scattering and its correlation with the [110] growth direction in gallium oxide nanowires. J. Appl. Phys. *98*, 094312.

Rao, A., Pundir, V.S., Tiwari, A., Padarthi, Y., Rao, N.V.M., Aich, S., and Roy, B. (2018). Investigating the effect of dopant type and concentration on TiO_2 powder microstructure via rietveld analysis. J. Phys. Chem. Sol. *113*, 164–176.

Sirleto, L., Ferrara, M.A., Nikitin, T., Novikov, S., and Khriachtchev, L. (2012). Giant Raman gain in silicon nanocrystals. Nat. Commun. *3*, 1220.

Song, Y.P., Zhang, H.Z., Lin, C., Zhu, Y.W., Li, G.H., Yang, F.H., and Yu, D.P. (2004). Luminescence emission originating from nitrogen doping of β-Ga_2O_3 nanowires. Phys. Rev. B *69*, 075304.

Stepanov, S.I., Nikolaev, V.I., Bougrov, V.E., and Romanov, A.E. (2016). Gallium oxide: properties and applications - a review. Rev. Adv. Mater. Sci. *44*, 63–86.

Volk, Y.V., Malyarevich, A.M., Yumashev, K.V., Alekseeva, I.P., Dymshits, O.S., Shashkin, A.V., and Zhilin, A.A. (2007). Stimulated emission of Co^{2+}-doped glass–ceramics. J. Non Cryst. Sol. *353*, 2408–2414.

Wang, T., Farvid, S.S., Abulikemu, M., and Radovanovic, P.V. (2010). Size-tunable phosphorescence in colloidal metastable γ-Ga_2O_3 nanocrystals. J. Am. Chem. Soc. *132*, 9250–9252.

Xia, M., Luo, J., Chen, C., Liu, H., and Tang, J. (2019). Semiconductor quantum dots-embedded inorganic glasses: fabrication, luminescent properties, and potential applications. Adv. Opt. Mater. *7*, 1900851.

Xie, C., Lu, X., Tong, X., Zhang, Z., Liang, F., Liang, L., Luo, L., and Wu, Y. (2019). Recent progress in solar-blind deep-ultraviolet photodetectors based on inorganic ultrawide bandgap semiconductors. Adv. Funct. Mater. *29*, 1806006.

Yang, M., Liu, X.J., Ruan, H.H., Wu, Y., Wang, H., and Lu, Z.P. (2016). High thermal stability and sluggish crystallization kinetics of high-entropy bulk metallic glasses. J. Appl. Phys. *119*, 245112.

Yue, Y., Shao, C., Kang, S., Wang, F., Wang, X., He, D., Chen, W., and Hu, L. (2018). Relationship investigation of structure and properties of Nd^{3+}: Ga_2O_3-Al_2O_3-PbO-CaO via Raman, infrared, NMR and EPR spectroscopy. J. Non Cryst. Sol. *499*, 201–207.

Zhang, J., Li, B., Xia, C., Pei, G., Deng, Q., Yang, Z., Xu, W., Shi, H., Wu, F., Wu, Y., et al. (2006). Growth and spectral characterization of β-Ga_2O_3 single crystals. J. Phys. Chem. Sol. *67*, 2448–2451.

Zhou, X.T., Heigl, F., Ko, J.Y.P., Murphy, M.W., Zhou, J.G., Regier, T., Blyth, R.I.R., and Sham, T.K. (2007). Origin of luminescence from Ga_2O_3 nanostructures studied using x-ray absorption and luminescence spectroscopy. Phys. Rev. B *75*, 125303.

Zhou, S., Li, C., Yang, G., Bi, G., Xu, B., Hong, Z., Miura, K., Hirao, K., and Qiu, J. (2013). Self-limited nanocrystallization-mediated activation of semiconductor nanocrystal in an amorphous solid. Adv. Funct. Mater. *23*, 5436–5443.

iScience, Volume *24*

Supplemental Information

In situ and tunable structuring of semiconductor-in-glass transparent composite

Liting Lin, Rulin Miao, Wenqiang Xie, Jiejie Chen, Yujun Zhao, Zhenping Wu, Jianrong Qiu, Haohai Yu, and Shifeng Zhou

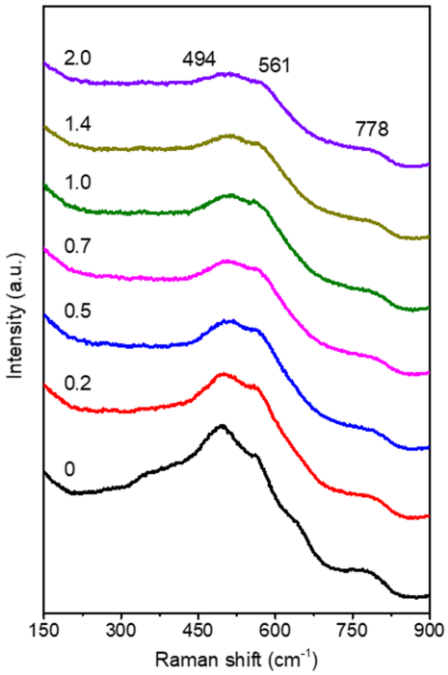

Figure S1. Raman spectra of as-made glass with various Al_2O_3/Ga_2O_3 ratio. The characteristic peaks at 494, 561and 778 cm^{-1} can be assigned to the regular $[Ga_2O_6]/[Al_2O_6]$, the vibrations of the bridged oxygen Ga-O-Ga/Al-O-Al linkages and $[GaO_4]/[AlO_4]$ structure units, respectively (Rao et al., 2005; Yue et al., 2018.). Related to Figure 1.

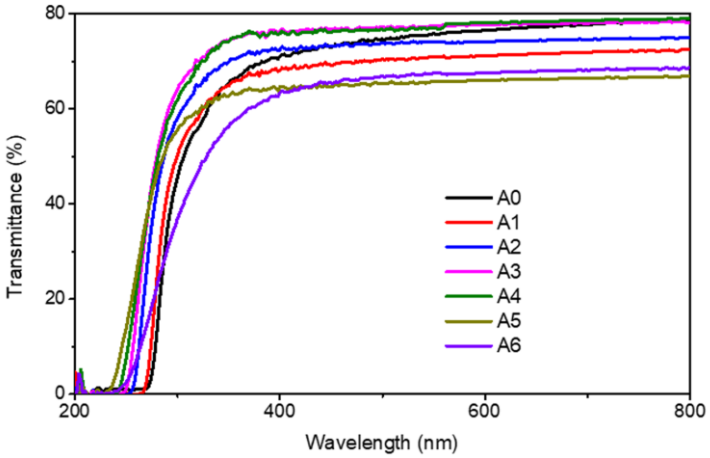

Figure S2. Transmission spectra of transparent composites with various Al_2O_3/Ga_2O_3 ratio. Related to Figure 2.

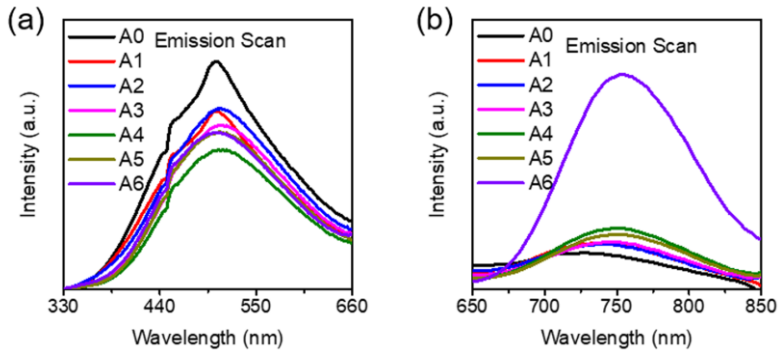

Figure S3. Optical properties of transparent composites. a) The blue-green luminescence of composites. b) The red luminescence of composites. Related to Figure 2.

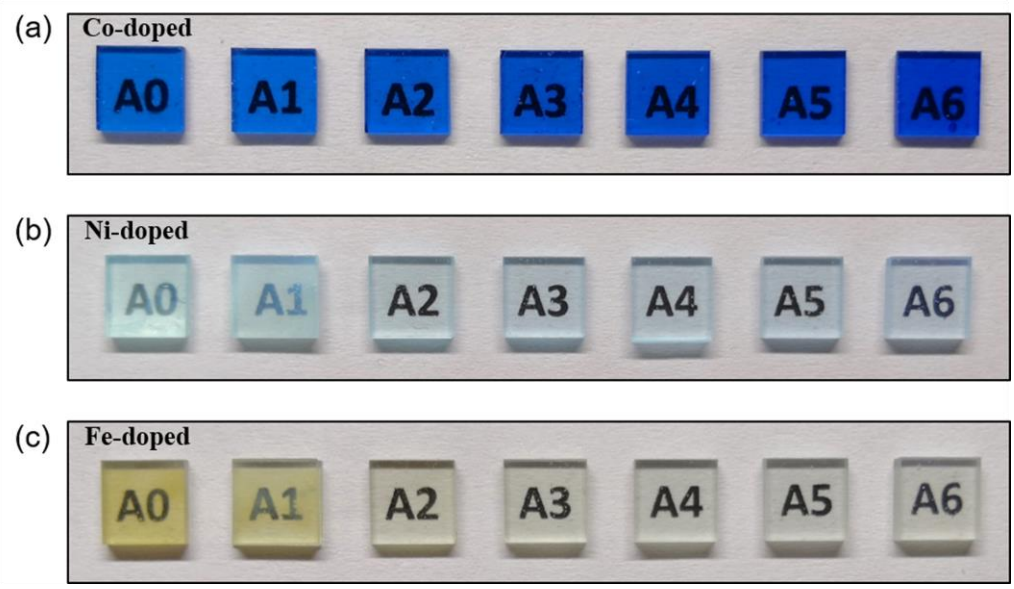

Figure S4. Photographs of the Co-doped (a), Ni-doped (a) and Fe-doped (c) transparent composites. Related to Figure 3.

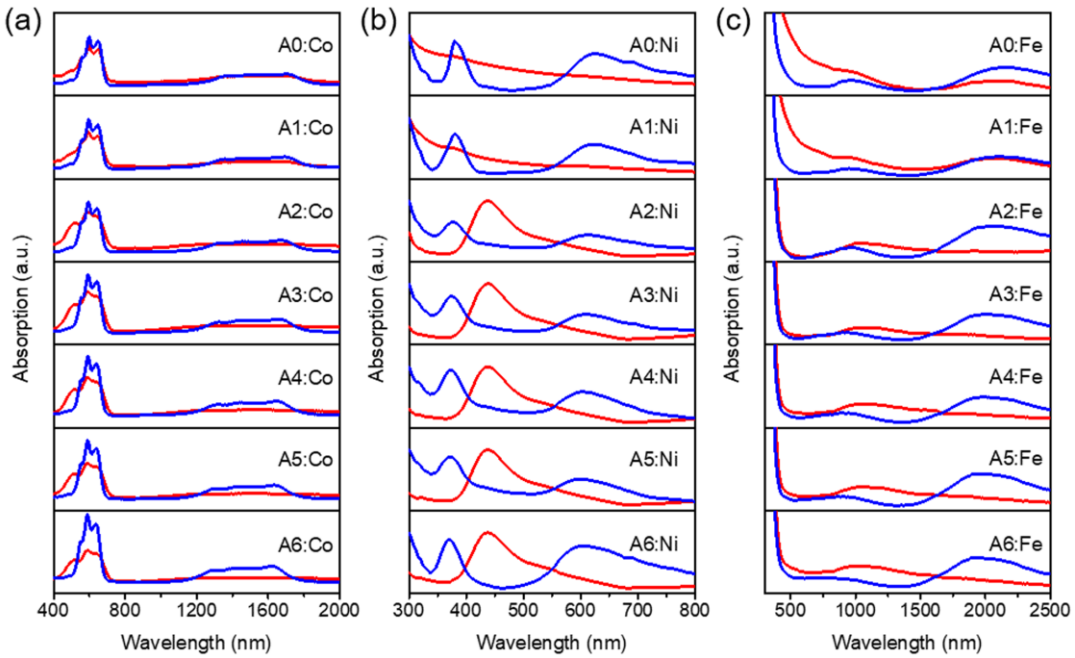

Figure S5. The absorption spectra of as-made glass (red line) and composite (blue line) doped with Co (a), Ni (b) and Fe (c). Related to Figure 3.

Table S1. Estimated crystal field parameters and fitted energy levels of Co^{2+} in transparent composites. Related to Figure 3.

		Dq	B	$^4A_2(^4F)\rightarrow {}^4T_1(^4F)$	$^4A_2(^4F)\rightarrow {}^2E(^2G)$	$^4A_2(^4F)\rightarrow {}^4T_1(^4P)$	$^4A_2(^4F)\rightarrow {}^2A_1(^2G)$
A0:Co	Expt. [cm^{-1}]			6476.68	15455.95	16750.42	17889.09
	Fitted [cm^{-1}]	372.05	804.36	6483.1	15774.62	16755.52	17802.05
A1:Co	Expt. [cm^{-1}]			6527.42	15503.88	16806.72	17921.15
	Fitted [cm^{-1}]	375.07	805.47	6517.55	15813.07	16821.69	17804.66
A2:Co	Expt. [cm^{-1}]			6605.02	15576.32	16863.41	18018.02
	Fitted [cm^{-1}]	379.73	805.11	6617.16	15784.63	16891.05	17865.05
A3:Co	Expt. [cm^{-1}]			6653.36	15600.62	16891.89	18018.02
	Fitted [cm^{-1}]	382.64	804.4	6675.38	15792.15	16910.4	17883.54
A4:Co	Expt. [cm^{-1}]			6697.92	15649.45	16949.15	18083.18
	Fitted [cm^{-1}]	385.28	805.91	6687.84	15800.24	16941.97	17981.06
A5:Co	Expt. [cm^{-1}]			6752.19	15698.59	16977.93	18115.94
	Fitted [cm^{-1}]	388.56	804.88	6747.66	15780.14	17018.63	17992.34
A6:Co	Expt. [cm^{-1}]			6802.72	15723.27	17006.8	18148.82
	Fitted [cm^{-1}]	391.62	804.06	6809.08	15764.12	17001.36	17974.09

Transparent Methods

Materials

The as-made glass with the composition (in mol%) of $53SiO_2$-$(30-x)Ga_2O_3$-xAl_2O_3-$7Na_2O$-10MgO, where x = 0, 5, 10, 12.5, 15, 17.5 and 20, respectively, were prepared by the classic melt-quenching method. The transition-metal ions species (Co, Ni, and Fe) (0.002 wt%) which act as active dopants were introduced into as-made glass. The high purity SiO_2, Ga_2O_3, Al_2O_3, Na_2O, MgO, CoO, NiO, and Fe_2O_3 were used as the raw materials. Approximate 30 g batches of raw materials were homogeneously mixed and melted in a corundum crucible at 1600 ^oC for 30 min in ambient atmosphere. Then the melt was poured on the copper plate to form transparent glass. Subsequently, the as-made glass samples were heat-treated at 850 ^oC for 2 h to form transparent composites (denoted as A0, A1, A2, A3, A4, A5 and A6 for Al_2O_3/Ga_2O_3 ratio of 0, 0.2, 0.5, 0.7, 1.0, 1.4 and 2, respectively). The samples were cut into pieces and polished for optical measurements.

Characterization

The X-ray diffraction (XRD) measurement was carried out to identify the crystalline phase and calculate the crystalline size and mass fraction. It was performed on a PANalytical X'Pert Pro X-ray diffractometer with Cu/Kα radiation at 40 mA and 40 kV (λ = 1.5406 Å). The crystalline size of semiconductor domain was evaluated by Scherrer formula according to the XRD diffraction peak broadening, and the crystalline mass fraction was calculated from the crystalline/amorphous areas of the X-ray diffractogram. Transmission electron microscope (TEM) was used to examine the microstructures of the samples which was performed on a FEI Tecnai G2 F20 with a field emission gun operated at 200 kV. The Raman measurement was conducted on the Renishaw inVia Raman spectrometer with the 532 nm laser as the excitation source. Absorption spectra were recorded on a Lambda 900 UV/VIS/NIR

spectrophotometer. Visible and infrared luminescence spectra were recorded on an Edinburgh Instruments FLS980 spectrometer and FLS920 fluorescence spectrometer, respectively.

Laser Experiments

A fiber-coupled semiconductor laser with a center wavelength of 795 nm was used as the pump source. The coupled fiber core diameter is 400 μm and the numerical aperture is 0.22. A Tm-doped $YAlO_3$ (Tm:YAP) crystal was utilized as the laser gain medium. The a-cut Tm:YAP crystal with dimensions of 3 × 3 × 10 mm was chose as the gain material and the two ends were laser-grade polished. The laser cavity was a traditional plano-concave design, in which the input mirror M1 is plated with the high transmission of the pump light at 795 nm and high reflection to the laser band. The plano-concave mirror with a radius of curvature of 50 mm, which has a 3% transmittance at 2 μm, was used as the output coupler M2. The Tm:YAP crystal was wrapped in indium foil and installed on a copper block which was maintained at a temperature of 10 °C by circulating water. Fe-doped transparent composite was inserted into the laser cavity as a Q-switched optical switch. In order to obtain a larger adjustment range, the sample was placed near the output coupling mirror M2. The cavity length was finally optimized to be about 45 mm in the following experiments. The laser output power, laser spectrum, pulse repetition frequency and pulse width were measured and recorded by power meter (Newport, model 1916-R), spectrometer (Optical Spectrum Analyzer OSA 205) and digital oscilloscope (Tektronix, MSO 72504DX), respectively.

Theoretical Simulations

The first-principles calculations were performed based on the density functional theory, by using the Vienna *ab initio* simulation package (VASP) code (Kresse and Furthmuller, 1996.). The projector augmented-wave (PAW) (Hohenberg and Kohn, 1964; Kohn and Sham, 1965.) method was employed with the Perdew-Burke-Ernzerhof (PBE) (Perdew et al., 1996.) type generalized gradient approximation (GGA) for describing the exchange-correlation potential. The cut-off energy of a plane-wave basis set was 520 eV with the energy convergence within

10^{-5} eV. The reciprocal space integrations were sampled with a Gamma centered mesh of 4 × 4 × 4 obtained by the Monkhorst-Pack method (Monkhorst and Pack, 1976.). We adopted DFT-1/2 method to obtain more accurate bandgaps with respect to the conventional gap-underestimation functional (Ferreira et al., 2008.). The optimal values of CUT for DFT-1/2 selected for O p orbital was 2.67 (Ferreira et al., 2008.). In our calculation model, the doping concentration of Co atom in Ga_2O_3 was 1.88 %, and the concentration of Al in Co:Ga_2O_3 was 1.85%.

References

Rao, R. F., Rao, A. M., Xu, B., Dong, J., Sharma, S., and Sunkara, M. K. (2005). Blueshifted Raman scattering and its correlation with the [110] growth direction in gallium oxide nanowires. J. Appl. Phys. *98*, 094312.

Yue, Y., Shao, C., Kang, S., Wang, F., Wang, X., He, D., Chen, W., and Hu, L. (2018). Relationship investigation of structure and properties of Nd^{3+}: Ga_2O_3-Al_2O_3-PbO-CaO via Raman, infrared, NMR and EPR spectroscopy. J. Non-Cryst. Solids *499*, 201-207.

Kresse, G., and Furthmuller, J. (1996). Efficient iterative schemes for ab initio total-energy calculations using a plane-wave basis set. Phys. Rev. B Condens. Matter *54*, 11169-11186.

Hohenberg, P., and Kohn, W. (1964). Inhomogeneous electron gas. Phys. Rev. *136*, B864-B871.

Kohn, W., and Sham, L. J. (1965). Self-consistent equations including exchange and correlation effects. Phys. Rev. *140*, A1133-A1138.

Perdew, J. P., Burke, K., and Ernzerhof, M. (1996). Generalized gradient approximation made simple. Phys. Rev. Lett. *77*, 3865-3868.

Monkhorst, H. J., and Pack, J. D. (1976). Special points for Brillouin-zone integrations. Phys. Rev. B *13*, 5188-5192.

Ferreira, L. G., Marques, M., and Teles, L. K. (2008). Approximation to density functional theory for the calculation of band gaps of semiconductors. Phys. Rev. B *78*, 125116.